# Decoupled Fault-Tolerant Model Predictive Current Control for Dual Three-Phase PMSMs With Harmonic Compensation

Jia Cui, Jinghua Ji, Wenxiang Zhao, *Senior Member, IEEE*, Tao Tao, Linsen Huang, and Hongyu Tang

***Abstract*—This article proposes a decoupled fault-tolerant model predictive current control for a dual three-phase permanent magnet synchronous motor with harmonic compensation. The harmonics caused by nonsinusoidal back electromotive force can be well controlled under the open-circuit fault scenario by designing a harmonic closed-loop scheme. First, a decoupled predictive model and fault-tolerant voltage vectors are deduced based on a reduced-dimension matrix, which can eliminate the coupling issues between the harmonic and fundamental subspaces. Afterward, a uniform harmonic-free virtual vector is constructed by rearranging the irregular voltage vectors. More importantly, a virtual null vector is designed in the scheme, where the virtual null vector is effective in the harmonic subspace and has no components in the fundamental subspace. So, the harmonics can be further controlled without affecting torque and flux generation. Extensive experimental results verify the effectiveness of the proposed method.**

***Index Terms*—Closed-loop, dual three-phase permanent magnet synchronous motors (DTP-PMSM), fault-tolerant model predictive current control (FTMPCC), open-circuit fault (OCF).**

## I. Introduction

COMPARED with the conventional three-phase motors, the most preferred feature of multiphase motors is good fault tolerance [1], [2], [3], [4]. This fault tolerance of *n*-phase motors is particularly appreciated in safety-critical applications, such as electric vehicles, aerospace, and ship propulsion. Among those multiphase motors, the multiple three-phase motors have been investigated widely because of the well-established three-phase technology [5], [6]. The simplest fault-tolerant control strategy for multiple three-phase motors is to disable the complete three-phase winding containing the faulty phase [7]. However, this strategy led to a significant power reduction. Therefore, the efficient fault-tolerant approach with no extra hardware has been a subject of intense research in recent years.

The finite control-set model predictive control (FCS-MPC, denote as MPC for simplicity) technique has proved to be a viable alternative to the vector control for multiphase drives, which avoids tuning the proportional–integral controllers and designing specific modulation techniques [8], [9], [10]. For the MPC scheme, all the candidate voltage vectors in the control set need to be evaluated by the predefined cost function. Although this is a time-consuming process, the computational burden is no longer the most intractable issue due to the rapid development of power devices and microprocessors. The relevant investigations have turned to performance improvement in recent years. The virtual-voltage vector (VV) based MPC is a common strategy to improve the harmonic suppression performance in multiphase machines, where the voltage vector components generated by the inverter in the harmonic subspace are equivalent to zero [11], [12], [13]. Furthermore, a null vector was inserted along with the selected active voltage vector in one control period to reduce torque ripple [14], [15]. Another variant of MPC was proposed in [16], [17], [18], where multiple vectors (two or more active vectors and one null vector) were used in the one control period based on duty cycle regulation. So, the operational performance can be improved since the modulation area was widened by using multiple vectors. However, the above-mentioned VV-based methods are actually open-loop control methods in the harmonic subspace. Thus, the harmonics caused by nonsinusoidal back electromotive force (EMF), mapped into the harmonic subspace using the vector space decomposition (VSD) method, were uncontrolled. In order to suppress the harmonics caused by the nonsinusoidal back EMF, Shao et al. [19], [20] injected a rotation vector into one control period by calculating the corresponding fifth and seventh components. Xu et al. [21] designed a novel switching-table-based direct torque control, where the *xy* current's closed loop with proportional–integral–resonant controllers is included. In [22], the VVs in two orthogonal subspaces were synthesized, which can simultaneously track the references in fundamental and harmonic spaces. However, all algorithms that control the harmonic subspace fail after an open-circuit fault (OCF) because the harmonic currents are coupled with the fundamental currents.

As mentioned above, the MPC is a control-set-based control method. The voltage vector in the control set directly affects

Manuscript received 14 June 2022; revised 16 August 2022; accepted 21 September 2022. Date of publication 28 September 2022; date of current version 18 November 2022. This work was supported in part by the National Natural Science Foundation of China under Grants 52025073 and in part by the Natural Science Foundation of Jiangsu Province under Grant BK20191225. Recommended for publication by Associate Editor R. Kennel. *(Corresponding author: Jinghua Ji.)*

Jia Cui, Jinghua Ji, Wenxiang Zhao, Tao Tao, and Linsen Huang are with the School of Electrical and Information Engineering, Jiangsu University, Zhenjiang 212013, China (e-mail: cuijia1030@qq.com; jjh@ujs.edu.cn; zwx@ujs.edu.cn; taotao0511@ujs.edu.cn; linsen.huang@qq.com).

Hongyu Tang is with the School of Electrical and Information, Zhenjiang College, Zhenjiang 212028, China (e-mail: t_redrain@163.com).

Color versions of one or more figures in this article are available at https://doi.org/10.1109/TPEL.2022.3210039.

Digital Object Identifier 10.1109/TPEL.2022.3210039

the control performance. However, the available degrees of freedom are reduced under the OCF scenario, which leads to the two orthogonal subspaces being dependent [23], [24], [25]. In order to avoid this conflict, the modification of the current references is required in the original control scheme [23], [26]. It is difficult to deduce the distribution of postfault voltage vectors because of the oscillation of the neutral point voltage and the back EMF generated by the faulty phase [27]. Several works have been done to explore the distribution of the voltage vector under the OCF scenario [27], [28], [29], [30]. It provides a theoretical basis for the development of follow-up research. On the other aspect, the displacement of the voltage vectors after the fault occurrence was analyzed in [31] for the dual three-phase permanent magnet synchronous motor (DTP-PMSM) system. Luo and Liu [32] proposed erratic control set for the MPC method without controller reconfiguration. However, those control sets are unsuitable for a harmonic closed-loop control system due to the coupled currents between the fundamental and harmonic subspaces. In addition, a VV-based MPC is adequate to cope with the coupled issues, which have been demonstrated as a disturbance-free control strategy for OCF fault in [31]. To sum up, the state-of-the-art research does not consider the control of the harmonic subspace for the multiphase machine under the OCF scenario. Also, for a DTP-PMSM, the postfault control set is variable due to the different configurations of the neutral point. Therefore, it is necessary to investigate the issues in the DTP-PMSM drive system, such as postfault control set, fault-tolerant VV, and postfault harmonic currents suppression.

This article proposes a decoupled fault-tolerant model predictive current control (FTMPCC). The position of the voltage vector can be accurately calculated regardless of the neutral point voltage and the faulty phase back EMF. Also, to continue suppressing the harmonic currents of the faulty DTP-PMSM, a closed-loop control scheme is designed for harmonic subspace with an elaborate VV control set. Compared with the conventional fault-tolerant method, the proposed FTMPCC can improve operational performance without causing coupling issues.

The rest of this article is organized as follows. The machine model and topology under prefault and postfault conditions are discussed in Section II. Then, the new virtual-vector control sets and harmonic closed-loop strategy are deduced in Section III. In Section IV, the experimental results are presented to verify the effectiveness of the proposed schemes. Section V concludes this article.

## II. Postfault Analysis of DTP-PMSM

The VSD technology is usually adopted to decouple the system under prefault conditions. Nevertheless, the relationship between variables will change after the OCF [23]. This section reveals the change and indicates the coupling issues of the DTP-PMSM control system.

In the healthy scenario, a six-order VSD matrix is employed to decouple the DTP-PMSM control system, which transforms the variables into three orthogonal stationary subspaces: $\alpha\beta$, $z_1z_2$, and $o_1o_2$ subspaces

$$T_{6s}=\frac{1}{6}\begin{bmatrix}2 & -1 & -1 & \sqrt{3} & -\sqrt{3} & 0\\ 0 & \sqrt{3} & -\sqrt{3} & 1 & 1 & -2\\ 2 & -1 & -1 & \sqrt{3} & -\sqrt{3} & 0\\ 0 & -\sqrt{3} & \sqrt{3} & 1 & 1 & -2\\ 2 & 2 & 2 & 0 & 0 & 0\\ 0 & 0 & 0 & 2 & 2 & 2\end{bmatrix}$$

$$\begin{bmatrix}f_\alpha & f_\beta & f_{z1} & f_{z2} & f_{o1} & f_{o2}\end{bmatrix}^T = T_{6s}\begin{bmatrix}f_A & f_B & f_C & f_D & f_E & f_F\end{bmatrix}^T. \quad (1)$$

Assuming the fault occurs in phase $F$, the corresponding phase current becomes zero ($i_F=0$), and the motor loses one degree of freedom.

It can be deduced from the six-order decoupled matrix that $i_F$ is not involved in $i_\alpha$, $i_{z1}$, and $i_{o1}$, so the current equation remains unchanged. However, the equations of $i_\beta$, $i_{z2}$, and $i_{o2}$ are influenced by $i_F$, and the relationship between the stationary subspace currents and phase currents can be expressed as follows:

$$\begin{cases} i_\beta=\left(\sqrt{3}i_B-\sqrt{3}i_C+i_D+i_E\right)/6\\ i_{z2}=\left(-\sqrt{3}i_B+\sqrt{3}i_C+i_D+i_E\right)/6\\ i_{o2}=(i_D+i_E)/3. \end{cases} \quad (2)$$

For two isolated neutrals, the constraints of the phase currents can be expressed as

$$\begin{cases} i_A+i_B+i_C=0\\ i_D+i_E=0\\ i_F=0. \end{cases} \quad (3)$$

Hence, the coupling issues can be deduced from (2) and (3)

$$\begin{cases} i_\beta=-i_{z2}\\ i_{o2}=0. \end{cases} \quad (4)$$

Since $i_\beta$ equals $-i_{z2}$, the $z_2$ components are no longer independent during fault. For a healthy DTP-PMSM, these harmonic currents are usually controlled to zero for loss minimization. However, during the OCF, an attempt to control those harmonic currents to zero will cause disruption in the $\beta$ current regulation.

## III. Proposed Control Method

The OCF reduces the degrees of freedom, which results in the coupling between the fundamental and harmonic subspaces. Hence, the conventional harmonics closed-loop control strategy will cause performance degradation. This section provides a decoupled FTMPCC based on a reduced-dimension decoupling strategy to cope with the coupling issues and improve the performance of DTP-PMSM.

### A. Model of the OCF Operation

As shown in Fig. 1, the DTP-PMSM is fed by a six-phase two-level voltage source inverter, which provides 32 switching states after an OCF occurs. These switching states can be expressed as a vector $\boldsymbol{v}_i=S_AS_BS_CS_DS_E$, where the $S_i$ ($i=A$, $B$, $C$, $D$, and

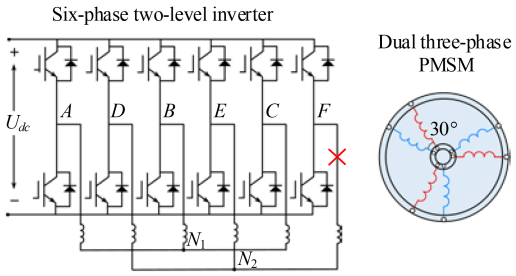


Fig. 1. Drive system of DTP-PMSM.

$E$) represents the switching state of the upper legs (ON is "1," while OFF is "0").

Using the reduced-dimension decoupling Clarke transformation matrix, the variables in the natural frame can be transformed into the stationary frame [33]

$$\begin{bmatrix} u_\alpha & u_\beta & u_z & u_{o1} & u_{o2} \end{bmatrix}^T = T_{5s} \begin{bmatrix} u_A & u_B & u_C & u_D & u_E \end{bmatrix}^T \tag{5}$$

where

$$T_{5s} = \frac{1}{3} \begin{bmatrix} 1 & -\frac{1}{2} & -\frac{1}{2} & \frac{\sqrt{3}}{2} & -\frac{\sqrt{3}}{2} \\ 0 & \frac{\sqrt{3}}{2} & -\frac{\sqrt{3}}{2} & 0 & 0 \\ 1 & -\frac{1}{2} & -\frac{1}{2} & -\frac{\sqrt{3}}{2} & \frac{\sqrt{3}}{2} \\ 1 & 1 & 1 & 0 & 0 \\ 0 & 0 & 0 & 1 & 1 \end{bmatrix}.$$

The zero-sequence subspace can be neglected because of the isolated neutrals configuration. Hence, the last two rows of $T_{5s}$ can be omitted, and (5) can be simplified as follows:

$$\begin{bmatrix} u_\alpha \\ u_\beta \\ u_z \end{bmatrix} = \frac{1}{3} \begin{bmatrix} 1 & -\frac{1}{2} & -\frac{1}{2} & \frac{\sqrt{3}}{2} \\ 0 & \frac{\sqrt{3}}{2} & -\frac{\sqrt{3}}{2} & 0 \\ 1 & -\frac{1}{2} & -\frac{1}{2} & -\frac{\sqrt{3}}{2} \end{bmatrix} \begin{bmatrix} u_A \\ u_B \\ u_C \\ u_{DE} \end{bmatrix}. \tag{6}$$

The $u_{DE}$ can be expressed by the switch state

$$[u_{DE}] = U_{dc} \begin{bmatrix} 1 & -1 \end{bmatrix} \begin{bmatrix} S_D & S_E \end{bmatrix}^T. \tag{7}$$

The relationship between $u_A$, $u_B$, and $u_C$ and the switch state can be expressed as

$$\begin{bmatrix} u_A \\ u_B \\ u_C \end{bmatrix} = \frac{U_{dc}}{3} \begin{bmatrix} 2 & -1 & -1 \\ -1 & 2 & -1 \\ -1 & -1 & 2 \end{bmatrix} \begin{bmatrix} S_A \\ S_B \\ S_C \end{bmatrix}. \tag{8}$$

Reorganized (7) and (8), $u_A, u_B, u_C$, and $u_{DE}$ can be expressed as

$$\begin{bmatrix} u_A \\ u_B \\ u_C \\ u_{DE} \end{bmatrix} = \frac{U_{dc}}{3} \begin{bmatrix} 2 & -1 & -1 & 0 & 0 \\ -1 & 2 & -1 & 0 & 0 \\ -1 & -1 & 2 & 0 & 0 \\ 0 & 0 & 0 & 3 & -3 \end{bmatrix} \begin{bmatrix} S_A \\ S_B \\ S_C \\ S_D \\ S_E \end{bmatrix}. \tag{9}$$

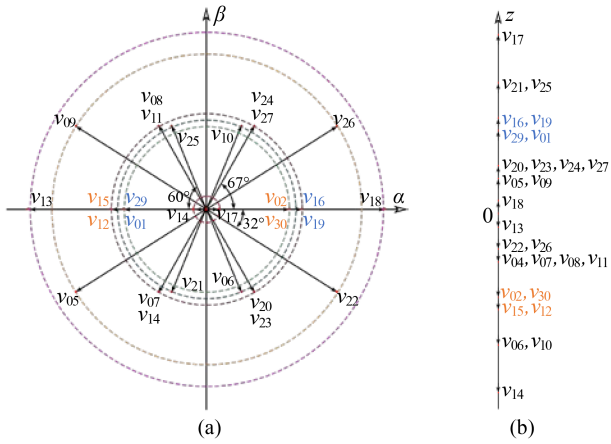


Fig. 2. Distributions of voltage vector under postfault conditions. (a) $\alpha\beta$-subspace. (b) $z$-axis.

TABLE I
SPECIFIC VALUE OF FAULT VOLTAGE VECTOR

| $v_i$ | $\alpha\beta$-subspace | $z$-axis | $v_i$ | $\alpha\beta$-subspace | $z$-axis |
|---|---|---|---|---|---|
| $v_{00}$ | $0e^{j0°}$ | $0e^{j0°}$ | $v_{16}$ | $0.333e^{j0°}$ | $0.333e^{j90°}$ |
| $v_{01}$ | $0.289e^{j180°}$ | $0.289e^{j90°}$ | $v_{17}$ | $0.045e^{j0°}$ | $0.622e^{j90°}$ |
| $v_{02}$ | $0.289e^{j0°}$ | $0.289e^{j-90°}$ | $v_{18}$ | $0.622e^{j0°}$ | $0.045e^{j90°}$ |
| $v_{03}$ | $0e^{j0°}$ | $0e^{j0°}$ | $v_{19}$ | $0.333e^{j0°}$ | $0.333e^{j90°}$ |
| $v_{04}$ | $0.333e^{j240°}$ | $0.167e^{j-90°}$ | $v_{20}$ | $0.333e^{j-60°}$ | $0.167e^{j90°}$ |
| $v_{05}$ | $0.539e^{j212°}$ | $0.122e^{j90°}$ | $v_{21}$ | $0.313e^{j247°}$ | $0.455e^{j90°}$ |
| $v_{06}$ | $0.313e^{j-67°}$ | $0.455e^{j-90°}$ | $v_{22}$ | $0.539e^{j-32°}$ | $0.122e^{j-90°}$ |
| $v_{07}$ | $0.333e^{j240°}$ | $0.167e^{j-90°}$ | $v_{23}$ | $0.333e^{j-60°}$ | $0.167e^{j90°}$ |
| $v_{08}$ | $0.333e^{j120°}$ | $0.167e^{j-90°}$ | $v_{24}$ | $0.333e^{j60°}$ | $0.167e^{j90°}$ |
| $v_{09}$ | $0.539e^{j148°}$ | $0.122e^{j90°}$ | $v_{25}$ | $0.313e^{j113°}$ | $0.455e^{j90°}$ |
| $v_{10}$ | $0.313\ e^{j67°}$ | $0.455e^{j-90°}$ | $v_{26}$ | $0.539e^{j32°}$ | $0.122e^{j-90°}$ |
| $v_{11}$ | $0.333e^{j120°}$ | $0.167e^{j-90°}$ | $v_{27}$ | $0.333\ e^{j60°}$ | $0.167e^{j90°}$ |
| $v_{12}$ | $0.333e^{j-180°}$ | $0.333e^{j-90°}$ | $v_{28}$ | $0e^{j0°}$ | $0e^{j0°}$ |
| $v_{13}$ | $0.622ej^{180°}$ | $0.045e^{j-90°}$ | $v_{29}$ | $0.289e^{j180°}$ | $0.289e^{j90°}$ |
| $v_{14}$ | $0.045ej^{180°}$ | $0.622e^{j-90°}$ | $v_{30}$ | $0.289e^{j0°}$ | $0.289e^{j-90°}$ |
| $v_{15}$ | $0.333ej^{180°}$ | $0.333e^{j-90°}$ | $v_{31}$ | $0e^{j0°}$ | $0e^{j0°}$ |

Form (6) and (9), the voltage of the stationary frame can be obtained by the switch state and expressed as follows:

$$\begin{bmatrix} u_\alpha \\ u_\beta \\ u_z \end{bmatrix} = \frac{U_{dc}}{3} \begin{bmatrix} 1 & -\frac{1}{2} & -\frac{1}{2} & -\frac{\sqrt{3}}{2} & \frac{\sqrt{3}}{2} \\ 0 & \frac{\sqrt{3}}{2} & -\frac{\sqrt{3}}{2} & 0 & 0 \\ 1 & -\frac{1}{2} & -\frac{1}{2} & \frac{\sqrt{3}}{2} & -\frac{\sqrt{3}}{2} \end{bmatrix} \begin{bmatrix} S_A \\ S_B \\ S_C \\ S_D \\ S_E \end{bmatrix}. \tag{10}$$

The phase voltages are eventually mapped into $\alpha\beta$-subspace and $z$-axis, which are shown in Fig. 2, with the specific values listed in Table I.

Finally, the $\alpha\beta$ variables can be expressed in the $dq$ reference frame by using the Park transformation matrix

$$P_{5s} = \begin{bmatrix} \cos\theta & \sin\theta & 0 & 0 & 0 \\ -\sin\theta & \cos\theta & 0 & 0 & 0 \\ 0 & 0 & 1 & 0 & 0 \\ 0 & 0 & 0 & 1 & 0 \\ 0 & 0 & 0 & 0 & 1 \end{bmatrix}. \tag{11}$$

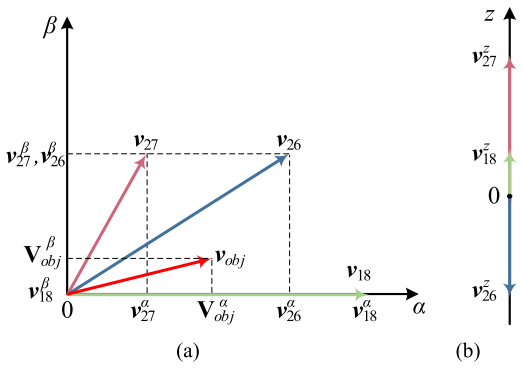


Fig. 3. Composition diagram of $\mathbf{V}_{\mathrm{obj}}$. (a) $\alpha\beta$-subspace. (b) $z$-axis.

The final mathematical model can be expressed as

$$\begin{aligned}\begin{bmatrix} u_d \\ u_q \end{bmatrix} &= R_s \begin{bmatrix} i_d \\ i_q \end{bmatrix} + \omega X \begin{bmatrix} 0 & -L_q \\ L_d & 0 \end{bmatrix} \begin{bmatrix} i_d \\ i_q \end{bmatrix} \\ &\quad + X \begin{bmatrix} L_d & 0 \\ 0 & L_q \end{bmatrix} \begin{bmatrix} di_d/dt \\ di_q/dt \end{bmatrix} + \omega \Psi_f X \begin{bmatrix} 0 \\ 1 \end{bmatrix} \\ u_x &= R i_x + L_l \frac{di_z}{dt} \\ T_e &= 3n_p((L_d - L_q) i_d i_q + \Psi_f i_q) \end{aligned} \tag{12}$$

where

$$X = \begin{bmatrix} 0.75 + 0.25\cos 2\theta & -0.25\sin 2\theta \\ -0.25\sin 2\theta & 0.75 - 0.25\cos 2\theta \end{bmatrix}.$$

### B. Construction of Fault-Tolerant Virtual Vector

According to Fig. 2, the basic voltage vectors can be used as the control sets for FCS-MPCC. However, those voltage vectors have components on the $z$-axis, which induce large harmonic currents. These harmonic currents can be suppressed by using multiple basic vectors to design a harmonic-free vector control set.

In this work, there are three active vectors with maximum magnitude selected to guarantee higher voltage utilization. According to the principle of multiple voltage vector synthesis, the relationships of virtual vector in the $\alpha$-axis, $\beta$-axis, and $z$-axis can be summarized as follows:

$$\begin{bmatrix} \mathbf{V}_i^{\alpha} \\ \mathbf{V}_i^{\beta} \\ \mathbf{V}_i^{z} \\ 1 \end{bmatrix} = \begin{bmatrix} v_{1st}^{\alpha} & v_{2nd}^{\alpha} & v_{3rd}^{\alpha} & 0 \\ v_{1st}^{\beta} & v_{2nd}^{\beta} & v_{3rd}^{\beta} & 0 \\ v_{1st}^{z} & v_{2nd}^{z} & v_{3rd}^{z} & 0 \\ 1 & 1 & 1 & 1 \end{bmatrix} \begin{bmatrix} D_1 \\ D_2 \\ D_3 \\ D_0 \end{bmatrix} \tag{13}$$

where $\boldsymbol{v}_{1\mathrm{st}}$, $\boldsymbol{v}_{2\mathrm{nd}}$, and $\boldsymbol{v}_{3\mathrm{rd}}$ represent the first, second, and third basic vectors, respectively. The superscripts $\alpha$, $\beta$, and $z$ represent the component of the $\alpha$-axis, $\beta$-axis, and $z$-axis of corresponding vectors, respectively. $D_i$ $(i = 0, 1, 2, 3)$ represents the ratio of the null vector, first vector, second vector, and third vector. $D_0, D_1, D_2, D_3 \in [0, 1]$.

Fig. 3 shows the composition diagram of the proposed fault-tolerant virtual vector. For an intuitive description, $\boldsymbol{v}_{18}$, $\boldsymbol{v}_{26}$, and $\boldsymbol{v}_{27}$ are used as examples. According to the geometric relations, the component of the objective vector ($\mathbf{V}_{\mathrm{obj}}$) in the $\alpha\beta$ axes can be described as follows:

$$\begin{cases} D_1 \cdot v_{18}^{\alpha} + D_2 \cdot v_{26}^{\alpha} + D_3 \cdot v_{27}^{\alpha} = \mathbf{V}_{\mathrm{obj}}^{\alpha} \\ D_1 \cdot v_{18}^{\beta} + D_2 \cdot v_{26}^{\beta} + D_3 \cdot v_{27}^{\beta} = \mathbf{V}_{\mathrm{obj}}^{\beta}. \end{cases} \tag{14}$$

Additionally, the principle of synthetic requires the virtual vector in harmonic subspace, which is zero. According to Fig. 3(b), $\boldsymbol{v}_{18}$, $\boldsymbol{v}_{27}$, and $\boldsymbol{v}_{26}$ in harmonic subspace pointed to different directions. So, the harmonic free can be satisfied by using the following equation:

$$D_1 \cdot v_{18}^{z} + D_2 \cdot v_{26}^{z} + D_3 \cdot v_{27}^{z} = \mathbf{V}_{\mathrm{obj}}^{z} = 0. \tag{15}$$

Finally, 12 equal magnitude virtual vectors with harmonic free are synthesized. The details of the synthesis principle are listed in Table II. Also, the distributions of the proposed fault-tolerant virtual vector are shown in Fig. 4. The angle between adjacent vectors of the new control set is 30°, and each virtual vector includes three basic active vectors and one null vector.

TABLE II
CONSTRUCTED FAULT-TOLERANT VIRTUAL VECTORS

| $\mathbf{V}_i$ | Voltage vector | | | | Ratios of each voltage vector | | | |
|---|---|---|---|---|---|---|---|---|
| $\mathbf{V}_i$ | $\boldsymbol{v}_{1\mathrm{st}}$ | $\boldsymbol{v}_{2\mathrm{nd}}$ | $\boldsymbol{v}_{3\mathrm{rd}}$ | $\boldsymbol{v}_0$ | $D_1$ | $D_2$ | $D_3$ | $D_0$ |
| $\mathbf{V}_1$ | $\boldsymbol{v}_{18}$ | $\boldsymbol{v}_{26}$ | $\boldsymbol{v}_{27}$ | $\boldsymbol{v}_{00}$ | 0.295 | 0.198 | 0.066 | 0.44 |
| $\mathbf{V}_2$ | $\boldsymbol{v}_{26}$ | $\boldsymbol{v}_{27}$ | $\boldsymbol{v}_{10}$ | $\boldsymbol{v}_{00}$ | 0.313 | 0.361 | 0.048 | 0.277 |
| $\mathbf{V}_3$ | $\boldsymbol{v}_{08}$ | $\boldsymbol{v}_{24}$ | $\boldsymbol{v}_{26}$ | $\boldsymbol{v}_{00}$ | 0.379 | 0.476 | 0.132 | 0.013 |
| $\mathbf{V}_4$ | $\boldsymbol{v}_{09}$ | $\boldsymbol{v}_{11}$ | $\boldsymbol{v}_{27}$ | $\boldsymbol{v}_{00}$ | 0.132 | 0.476 | 0.379 | 0.013 |
| $\mathbf{V}_5$ | $\boldsymbol{v}_{25}$ | $\boldsymbol{v}_{08}$ | $\boldsymbol{v}_{09}$ | $\boldsymbol{v}_{00}$ | 0.048 | 0.361 | 0.313 | 0.277 |
| $\mathbf{V}_6$ | $\boldsymbol{v}_{08}$ | $\boldsymbol{v}_{09}$ | $\boldsymbol{v}_{13}$ | $\boldsymbol{v}_{00}$ | 0.066 | 0.198 | 0.295 | 0.44 |
| $\mathbf{V}_7$ | $\boldsymbol{v}_{13}$ | $\boldsymbol{v}_{05}$ | $\boldsymbol{v}_{04}$ | $\boldsymbol{v}_{00}$ | 0.295 | 0.198 | 0.066 | 0.44 |
| $\mathbf{V}_8$ | $\boldsymbol{v}_{05}$ | $\boldsymbol{v}_{04}$ | $\boldsymbol{v}_{21}$ | $\boldsymbol{v}_{00}$ | 0.313 | 0.361 | 0.048 | 0.277 |
| $\mathbf{V}_9$ | $\boldsymbol{v}_{05}$ | $\boldsymbol{v}_{07}$ | $\boldsymbol{v}_{23}$ | $\boldsymbol{v}_{00}$ | 0.132 | 0.476 | 0.379 | 0.013 |
| $\mathbf{V}_{10}$ | $\boldsymbol{v}_{22}$ | $\boldsymbol{v}_{20}$ | $\boldsymbol{v}_{04}$ | $\boldsymbol{v}_{00}$ | 0.132 | 0.476 | 0.379 | 0.013 |
| $\mathbf{V}_{11}$ | $\boldsymbol{v}_{06}$ | $\boldsymbol{v}_{23}$ | $\boldsymbol{v}_{22}$ | $\boldsymbol{v}_{00}$ | 0.048 | 0.361 | 0.313 | 0.277 |
| $\mathbf{V}_{12}$ | $\boldsymbol{v}_{23}$ | $\boldsymbol{v}_{22}$ | $\boldsymbol{v}_{18}$ | $\boldsymbol{v}_{00}$ | 0.066 | 0.198 | 0.295 | 0.44 |

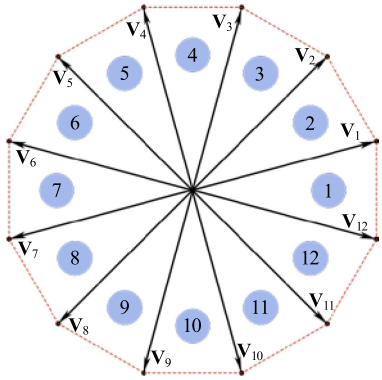


Fig. 4. Distributions of the proposed fault-tolerant virtual vectors.

### C. Harmonic Closed-Loop Control With Virtual Null Vectors (VNs)

The virtual-vector method is essentially a harmonic open-loop control scheme and has little restraint on harmonics. However, the harmonics caused by nonsinusoidal back EMF are transformed into harmonic subspace for the DTP-PMSM. In

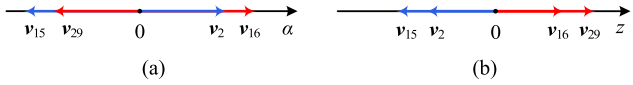


Fig. 5. Composition diagram VNs. (a) $\alpha\beta$-subspace. (b) $z$-axis.

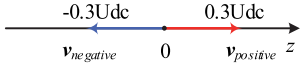


Fig. 6. Distributions of reconstructed VNs.

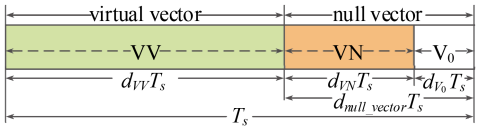


Fig. 7. Diagram of vector allocation in one control period.

this section, a VN is devised, which generates the harmonic compensation voltage to suppress the harmonic currents without affecting the fundamental variables.

As shown in Fig. 2, $\boldsymbol{v}_{15}$ and $\boldsymbol{v}_2$ are in opposite directions on the $\alpha$-axis, whereas $\boldsymbol{v}_{15}$ and $\boldsymbol{v}_2$ point in the same direction on the $z$-axis. So, the VN can be synthesized by allocating the action time of the $\boldsymbol{v}_{15}$ and $\boldsymbol{v}_2$. The composition diagram of VNs is shown in Fig. 5. Since the harmonic subspace becomes a one-dimensional (1-D) space after the OCF, there are two VNs that need to be synthesized. One is positive, and the other is negative. Therefore, $\boldsymbol{v}_{29}$ and $\boldsymbol{v}_{16}$ are selected to synthesize positive VN. The following synthesis principle can be obtained through geometric relationships:

$$\begin{cases} \boldsymbol{V}_{\text{positive}} = 0.536\boldsymbol{v}_{29} + 0.464\boldsymbol{v}_{16} \\ \boldsymbol{V}_{\text{negative}} = 0.536\boldsymbol{v}_{2} + 0.464\boldsymbol{v}_{15}. \end{cases} \tag{16}$$

As a result, two VNs in opposite directions on the $z$-axis are synthesized. As shown in Fig. 6, the magnitude is 0.3Udc and has no components on the $\alpha\beta$-subspace. The VN is not involved in electromechanical energy conversion but is responsible for harmonic regulation.

After determining VN, the harmonic subspace can be controlled by inserting the VN into the control period and eventually forming a harmonic closed-loop scheme. As shown in Fig. 7, the new scheme contains three parts in one period: fundamental subspace controlled by virtual vector, harmonic subspace controlled by VN, and remaining interval supplemented with null vector ($V_0$). The duty cycle of each vector is calculated in the following steps.

1) *Duty Cycle Calculation of Virtual Vector:* Since the fundamental variables are responsible for electromechanical energy conversion, the main control object in the proposed method is still the fundamental subspace. In this article, the deadbeat principle of the $q$-axis currents is adopted to calculate the duty cycle of the virtual vector. This principle can be expressed as

$$\begin{cases} i_q^* = i_q^k + s_{\text{VV}} \cdot d_{\text{VV}} T_s + s_{\text{null\_vector}} \cdot d_{\text{null\_vector}} T_s \\ d_{\text{VV}} + d_{\text{null\_vector}} = 1 \end{cases} \tag{17}$$

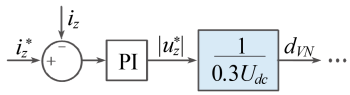


Fig. 8. Process of calculating the duty cycle of VN.

where "$*$" represents the reference value. $s_{\text{null\_vector}}$ and $s_{\text{VV}}$ are the slopes of $i_q$ under null vector and virtual-vector action. $d_{\text{null\_vector}}$ and $d_{\text{VV}}$ are the duty cycle of null vector and VV.

It should be noted that the null vector contains two parts, VN and $V_0$. Then, the duty cycle of null vector and virtual vector can be obtained as follows:

$$\begin{aligned} d_{\text{null\_vector}} &= \frac{i_q^* - i_q^k - s_{\text{VV}} T_s}{(s_{\text{null\_vector}} - s_{\text{VV}}) T_s} \\ d_{\text{VV}} &= \frac{i_q^* - i_q^k - s_{\text{null\_vector}} T_s}{(s_{\text{null\_vector}} - s_{\text{VV}}) T_s}. \end{aligned} \tag{18}$$

2) *Duty Cycle Calculation of VN:* Fig. 8 shows the process of calculating the duty cycle of VN, where a proportional-integral (PI) controller is used to obtain the reference voltage of the harmonic subspace (named $u_z^*$). According to the principle of voltage vector modulation in 1-D space, the duty cycle of VN is equal to the magnitude of $u_z^*$ divided by the magnitude of VN

$$d_{\text{VN}} = \left| \frac{u_z^*}{0.3U_{\text{dc}}} \right|. \tag{19}$$

In addition, considering the performance of the fundamental subspace, the $d_{\text{VN}}$ should be smaller than $(1-d_{\text{VV}})$, and the constraint is expressed as follows:

$$d_{\text{VN}} = \begin{cases} d_{\text{VN}}, & d_{\text{VN}} < 1 - d_{\text{VV}} \\ 1 - d_{\text{VV}}, & d_{\text{VN}} > 1 - d_{\text{VV}}. \end{cases} \tag{20}$$

3) *Duty Cycle Calculation of* $V_0$*:* After determining the duty cycle of the virtual vector and VN, the remaining duty cycle in one control cycle is allocated to $V_0$, and can be expressed as

$$d_{V_0} = 1 - d_{\text{VV}} - d_{\text{VN}}. \tag{21}$$

The $V_0$ in this article is defined as $S_A S_B S_C S_D S_E = 00000$. So, the final duty cycle of each phase leg can be expressed as

$$\begin{aligned} &\left[d_A^{\text{final}} \quad d_B^{\text{final}} \quad d_C^{\text{final}} \quad d_D^{\text{final}} \quad d_E^{\text{final}}\right]^T \\ &= d_{\text{VV}}\left[d_A^{\text{VV}} \quad d_B^{\text{VV}} \quad d_C^{\text{VV}} \quad d_D^{\text{VV}} \quad d_E^{\text{VV}}\right]^T \\ &\quad + d_{\text{VN}}\left[d_A^{\text{VN}} \quad d_B^{\text{VN}} \quad d_C^{\text{VN}} \quad d_D^{\text{VN}} \quad d_E^{\text{VN}}\right]^T \end{aligned} \tag{22}$$

where "final" represents the final duty cycles of each phase leg.

### D. Fault-Tolerant Predictive Model

The predictive model can be obtained by using the forward Euler formula to discretize (12). Additionally, a two-step prediction should be taken to compensate for the DSP system. Therefore,

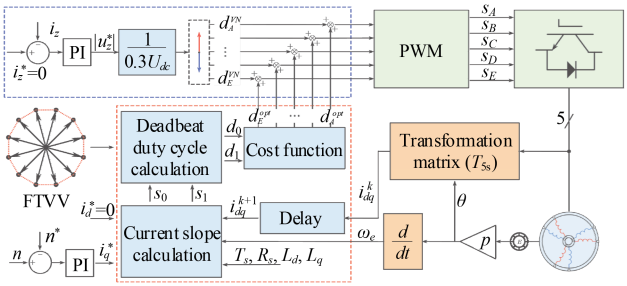


Fig. 9. Control block diagram of the proposed method.

the currents in the $dq$ axes at $k$+2 instant can be expressed as

$$\begin{cases} i_d^{k+2} = i_d^{k+1} + T_s\left[(1.5 - 0.5\cos 2\theta)\cdot\left(u_d^{k+1} - R_s i_d^{k+1}\right)\right. \\ \quad \left. + 0.5\sin 2\theta\cdot\left(u_q^{k+1} - R_s i_q^{k+1}\right) + \omega L_q i_q^{k+1}\right]/L_d \\ i_q^{k+2} = i_q^{k+1} + T_s\left[(1.5 + 0.5\cos 2\theta)\cdot\left(u_q^{k+1} - R_s i_q^{k+1}\right)\right. \\ \quad \left. + 0.5\sin 2\theta\cdot\left(u_d^{k+1} - R_s i_d^{k+1}\right) - \omega L_d i_d^{k+1} - \omega\Psi_r\right]/L_d \end{cases} \tag{23}$$

where the "$k$+1" and "$k$+2" represent the corresponding variables in $k$+1 and $k$+2 instant, respectively.

The cost function of FTMPCC can be expressed as follows, where the harmonic components are not included:

$$g = \left(i_d^* - i_d^{k+2}\right)^2 + \left(i_q^* - i_q^{k+2}\right)^2. \tag{24}$$

The proposed control block diagram is shown in Fig. 9. The harmonics control part is marked with a blue dotted box. This part generates the compensation duty cycles by the designed VN to suppress the harmonics caused by back EMF. In addition, the red dotted box is the fault-tolerant predictive model. The slope calculation is performed after the current variables are compensated by the delay module. Then, the duty cycle of each virtual vector can be obtained by (18) and used to modify the magnitude of the virtual vector. Afterward, all the modified virtual vectors are evaluated by the cost function to select the optimal vector and record the optimal duty cycle. Finally, the optimal duty cycles and compensation duty cycles constitute the final duty cycle. The inverter outputs the final duty cycles to drive the DTP-PMSM.

## IV. Experimental Verification

An experimental platform is established to verify the proposed method, as shown in Fig. 10. A surface-mounted DTP-PMSM is fed by a six-phase voltage source inverter. The magnetic power brake is used as the load. All algorithms are implemented by using the TMS320F28377 digital signal processor. The main parameters of the DTP-PMSM are listed in Table III. The virtual-vector-based FCS-MPCC with the back EMF compensation is selected for comparison (named M1 for simplicity) [22]. The proposed method without VN is named M2, and the proposed method with VN is named M3.

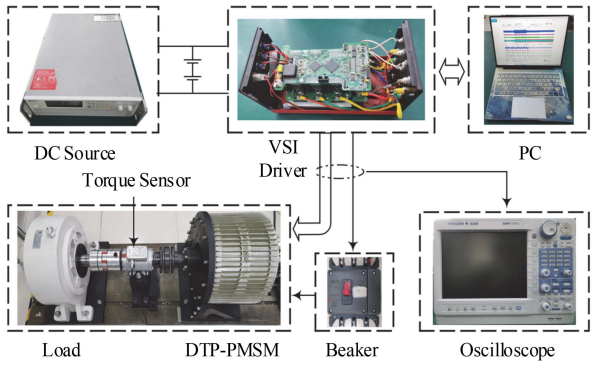


Fig. 10. Experimental platform.

TABLE III
Parameters of Experimental Motor and Drives System

| Parameters | Value | Unit |
|---|---|---|
| $\alpha\beta$-axes inductances | 15.4 | mH |
| Rotor flux | 0.88 | Wb |
| Stator resistance | 0.9 | Ω |
| Number of pole pairs | 11 | / |
| Rated torque | 150 | N.m |
| Sample frequency | 10 | kHz |
| DC Bus Voltage | 200 | V |

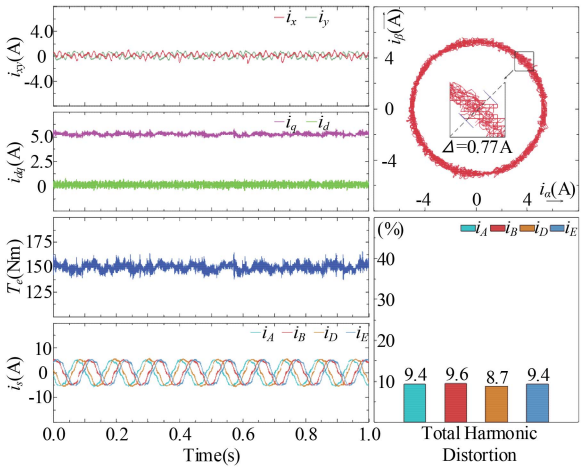


Fig. 11. Steady-state performance of M1 under prefault conditions.

TABLE IV
Steady-State Performance of Different Methods

| | $T_{e\ ripple}$ | $i_{d\ ripple}$ | $i_{q\ ripple}$ | $i_{x\ ripple}$ | $i_{y\ ripple}$ |
|---|---|---|---|---|---|
| M1(pre-fault) | 3.84 N.m | 0.18 A | 0.13 A | 0.36 A | 0.43 A |
| M1(post-fault) | 7.21 N.m | 0.27 A | 0.19 A | 1.94 A | 3.52 A |
| M2(without VN) | 3.78 N.m | 0.22 A | 0.13 A | 0.46 A($i_z$) | / |
| M3(with VN) | 3.54 N.m | 0.14 A | 0.12 A | 0.29 A($i_z$) | / |

### A. Steady-State Performance

Figs. 11–14 show the experimental results of steady-state performance. For detailed quantitative analysis, the total harmonic distortion (THD) analysis is calculated, where the original data are recorded from the experiment. Also, Table IV lists the results of torque and current ripple, which are calculated by the

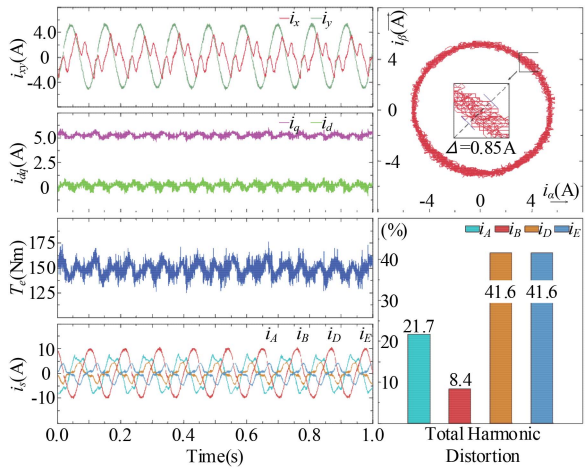


Fig. 12. Steady-state performance of M1 under postfault conditions.

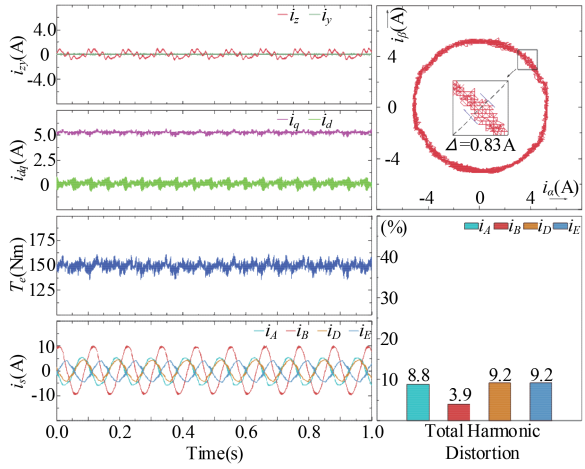


Fig. 13. Steady-state performance of M2.

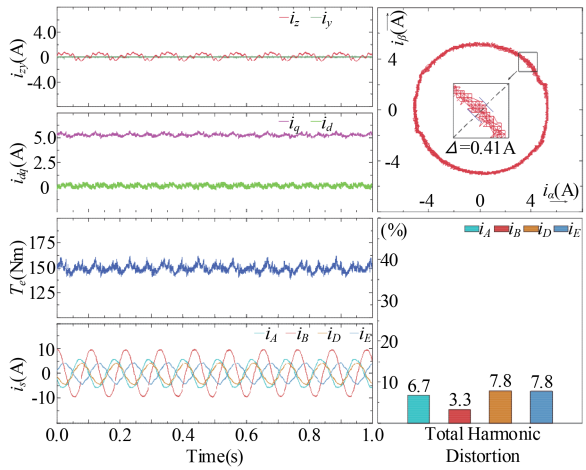


Fig. 14. Steady-state performance of M3.

following:

$$X_{\text{ripple}} = \sqrt{\frac{1}{n}\sum_{i=1}^{n}\left(X_i - \overline{X}\right)^2} \tag{25}$$

where $X$ represents the $xy$ axes' currents, $dq$ axes' currents, and electromagnetic torque in this article, respectively.

Fig. 11 shows the steady-state performance of M1 when the DTP-PMSM is under prefault conditions. In this experiment, the reference speed is 50 r/min, and the load is 150 N·m. As shown in Fig. 11, the phase currents are sinusoidal, and the THD of $i_A$, $i_B$, $i_D$, and $i_E$ is 9.4%, 9.6%, 8.7%, and 9.4%, respectively. It can be observed that the current of the $d$-axis is around zero due to the $i_d = 0$ method being adopted. The motor is well controlled using the harmonic closed-loop control method, and the ripples of $i_x$, $i_y$, $i_d$, and $i_q$ are 0.36 A, 0.43 A, 0.18 A, and 0.13 A, respectively. The torque ripple is 3.84 N·m at the same time. Also, since two orthogonal subspaces are considered in M1, the $\alpha\beta$ currents have a circular trajectory. Fig. 12 shows postfault performance when phase $F$ is disconnected. It can be noted that the amplitude of $i_B$ is increased, and the other phase currents are distorted. The THD of $i_A$, $i_B$, $i_D$, and $i_E$ is 21.7%, 41.6%, and 41.6%, respectively. In addition, the $i_x$ displays a heavy pulsation and $i_y$ presents a sinusoidal waveform. This is because the $i_y$ is coupled to $i_\beta$, and the value of $i_y$ equals $-i_\beta$ in the OCF. Controlling the harmonic subspace affects the performance of electromechanical energy conversion, and the torque ripples are 7.2 N·m. Similar deteriorations are also exhibited in $i_{dq}$ and $i_{\alpha\beta}$. This means the coupling issues exist in the OCF with the convention transformation matrix.

In order to verify the effectiveness of the proposed decoupling virtual vector, the experiments of the proposed FTMPCC with and without VN are conducted. The steady-state performance of M2 is shown in Fig. 13. Results show that the $i_y$ vanished due to the reduced control freedom, and the harmonic currents are reduced simultaneously. In addition, the phase currents are significantly improved. The THD of $i_A$, $i_B$, $i_D$, and $i_E$ is 8.8%, 3.9%, 9.2%, and 9.2%, respectively. Also, the torque and $dq$ currents' ripples are reduced and comparable to normal conditions. This is because the reduced-dimension matrix is orthogonal among $\alpha$–$\beta$, $\alpha$–$z$, and $\beta$–$z$. So, the coupling issues are solved. This means the proposed strategy can effectively remedy the operational performance under the OCF conditions. Fig. 14 presents the steady-state performance of M3, where the VN is enabled. It can be seen that M3 provides satisfactory performance in postfault situations. The harmonic current is smaller than the results presented in M2. The phase currents are more sinusoidal, and the THD is superior to M2. The torque ripple is 3.54 N·m, and the $dq$ currents' ripples are 0.14 A and 0.12 A, respectively. In addition, the $\alpha\beta$ currents trajectory becomes more delicate than the other methods. This is because the compensation module further regulates the harmonic currents. The influence of back EMF can be remedied through the designed harmonic closed-loop control system.

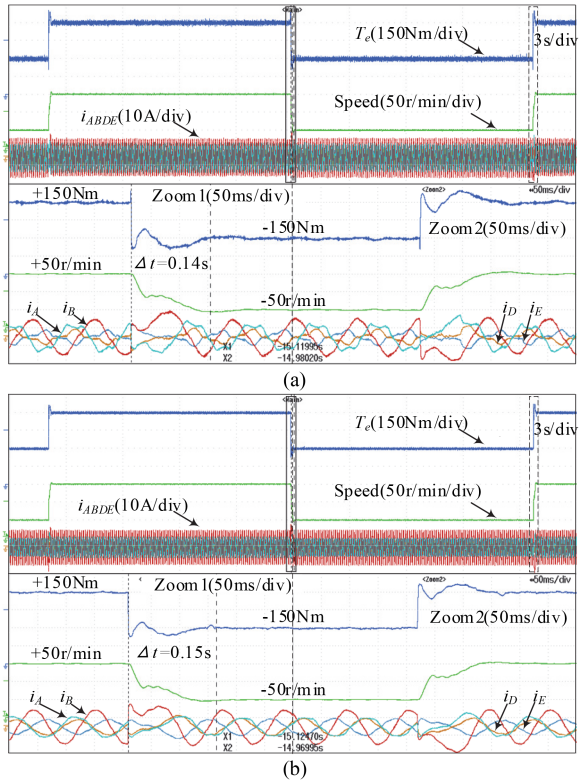


Fig. 15. Dynamic performance. (a) M1. (b) M3.

## B. Dynamic Performance

Fig. 15 shows the experimental result of the dynamic performance, where the reference speed changes from +50 to −50 r/min. The waveforms of actual speed, phase current, and torque are depicted. As shown in Fig. 15(a), the conventional FCS-MPCC can quickly track the speed reference, and the dynamic process lasts 0.14 s. In Fig. 15(b), the transient process of the proposed method is similar to the conventional FCS-MPCC. The excellent dynamic performance is guaranteed. Also, the steady-state performance of the proposed method is significantly improved under different speeds.

The parameter sensitivity is investigated in this section. In this experiment, the *dq* axes' inductances, rotor flux, and stator resistors of the predictive model are changed in the algorithm. The experimental results are exhibited in Figs. 16–18, where the parameters increase from the accurate value to 150% and then decrease to 50%. It can be seen from Fig. 16 that the torque is not affected when the *dq* axes increase. However, the performance is slightly disturbed when the *dq* axes' inductances decrease. This effect corresponds to the analysis of the article presented in [28]. In Fig. 17, the actual speed and torque are slightly influenced and return to the reference value quickly. It can be concluded from Fig. 18 that the performance is not affected by the mismatched stator resistance. Thus, the proposed method has good robustness.

The transition from prefault to postfault operation with different methods is shown in Fig. 19. In this experiment, the DTP-PMSM is operated in normal situation for a few seconds. Then, phase *F* is disconnected by using a breaker. After about

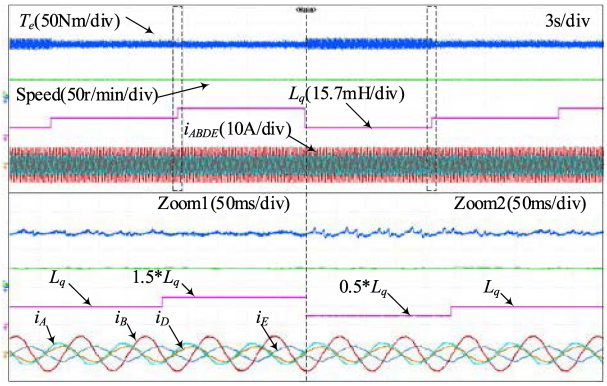


Fig. 16. Performance of the inductance variations for the proposed method.

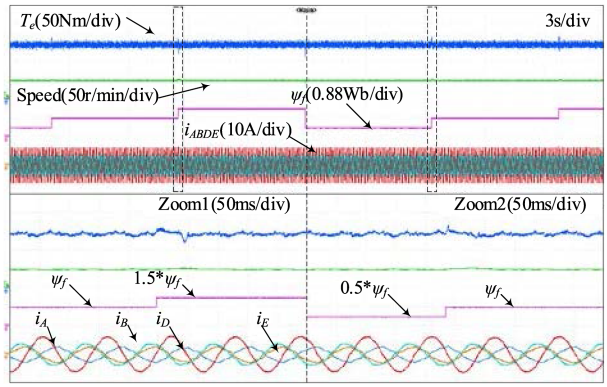


Fig. 17. Performance of the rotor flux variations for the proposed method.

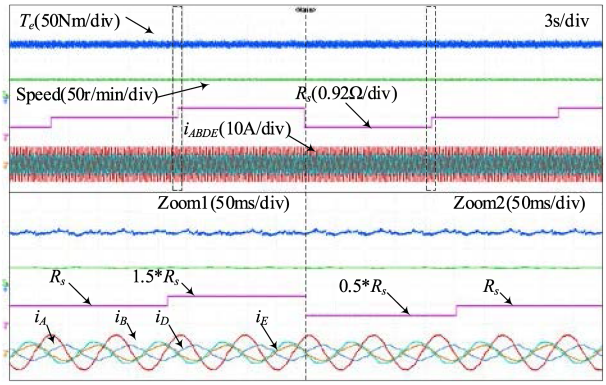


Fig. 18. Performance of the stator resistance variations for the proposed method.

12.5 s, the proposed method without compensation is used. Finally, the proposed method with harmonic compensation is implemented. The waveforms of *dq* currents, phase currents, and torque are recorded. It can be seen from Fig. 19 that the *dq* currents, phase currents, and torque can be well controlled under prefault conditions. When an OCF occurs, the current amplitude of the healthy phase is increased. Also, the ripples of *dq* currents and torque are increased. After adopting the constructed virtual-vector control set, the operational performance is improved. However, the ripples of the *d*-axis current

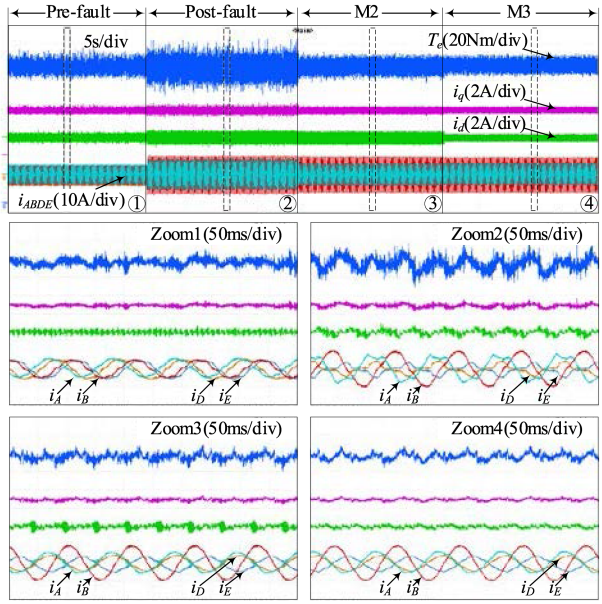


Fig. 19. Transition from prefault to postfault performance.

are still large. This situation can be improved by introducing the proposed compensation module. The final phase currents become sinusoidal, and the ripple of *dq* currents and torque is comparable with normal conditions. The transition experiments indicate that the proposed method is feasible, and the faulty drive can realize continuous operation without downtime.

## V. Conclusion

In this article, a decoupled FTMPCC has been investigated and implemented. The proposed method is characterized by the simultaneous consideration of nonsinusoidal back EMF harmonics and inverter-generated harmonic voltage vectors. The harmonic currents are decoupled with fundamental currents under the OCF scenario for DTP-PMSM by using the proposed method. Hence, the deduced voltage vector distributions and devised predictive model are fault tolerant. Also, a fault-tolerant virtual-vector control set with harmonic free is constructed. So, the harmonics caused by inverter-generated vectors can be canceled. In addition, a harmonic closed-loop scheme is designed to suppress the harmonics caused by nonsinusoidal back EMF, where the VN can control the harmonic subspace without affecting the fundamental variables. Experimental results show that the proposed method has better steady-state performance than the conventional method and can maintain good dynamic performance and robustness.

## References

[1] J. Xu, M. Odavic, Z.-Q. Zhu, Z.-Y. Wu, and N. M. A. Freire, "Modulation restraint analysis of space vector PWM for dual three-phase machines under vector space decomposition," *IEEE Trans. Power Electron.*, vol. 36, no. 12, pp. 14491–14507, Dec. 2021.

[2] F. Barrero and M. J. Duran, "Recent advances in the design, modeling, and control of multiphase machines—Part I," *IEEE Trans. Ind. Electron.*, vol. 63, no. 1, pp. 449–458, Jan. 2016.

[3] M. J. Duran and F. Barrero, "Recent advances in the design, modeling, and control of multiphase machines—Part II," *IEEE Trans. Ind. Electron.*, vol. 63, no. 1, pp. 459–468, Jan. 2016.

[4] S. Saeed, W. Zhao, H. Wang, T. Tao, and F. Khan, "Fault-tolerant deadbeat model predictive current control for a five-phase PMSM with improved SVPWM," *Chin. J. Elect. Eng.*, vol. 7, no. 3, pp. 111–123, Sep. 2021.

[5] G. Liu, M. Zhao, Q. Chen, W. Zhao, and X. Zhu, "Performance comparison of fault-tolerant control for triple redundant 3 × 3-phase motors driven by mono-inverter," *IEEE Trans. Transp. Electrific.*, vol. 8, no. 2, pp. 1839–1852, Jun. 2022.

[6] V. F. M. B. Melo, C. B. Jacobina, N. Rocha, and E. R. Braga-Filho, "Fault tolerance performance of two hybrid six-phase drive systems under single-phase open-circuit fault operation," *IEEE Trans. Ind. Appl.*, vol. 55, no. 3, pp. 2973–2983, May/Jun. 2019.

[7] E. Jung, H. Yoo, S.-K. Sul, H.-S. Choi, and Y.-Y. Choi, "A nine-phase permanent-magnet motor drive system for an ultrahigh-speed elevator," *IEEE Trans. Ind. Appl.*, vol. 48, no. 3, pp. 987–995, May/Jun. 2012.

[8] F. Barrero, M. R. Arahal, R. Gregor, S. Toral, and M. J. Duran, "A proof of concept study of predictive current control for VSI-driven asymmetrical dual three-phase ac machines," *IEEE Trans. Ind. Electron.*, vol. 56, no. 6, pp. 1937–1954, Jun. 2009.

[9] M. Bermúdez, C. Martin, I. González-Prieto, M. J. Duran, M. R. Arahal, and F. Barrero, "Predictive current control in electrical drives: An illustrated review with case examples using a five-phase induction motor drive with distributed windings," *IET Electr. Power Appl.*, vol. 14, pp. 1291–1310, Aug. 2020.

[10] H. Hadla and F. Santos, "Performance comparison of field-oriented control, direct torque control, and model-predictive control for SynRMs," *Chin. J. Elect. Eng.*, vol. 8, no. 1, pp. 24–37, Mar. 2022.

[11] Y. Ren and Z. Q. Zhu, "Enhancement of steady-state performance in direct-torque-controlled dual three-phase permanent-magnet synchronous machine drives with modified switching table," *IEEE Trans. Ind. Electron.*, vol. 62, no. 6, pp. 3338–3350, Jun. 2015.

[12] I. Gonzalez-Prieto, M. J. Duran, J. J. Aciego, C. Martin, and F. Barrero, "Model predictive control of six-phase induction motor drives using virtual voltage vectors," *IEEE Trans. Ind. Electron.*, vol. 65, no. 1, pp. 27–37, Jan. 2018.

[13] P. F. C. Gonçalves, S. M. A. Cruz, and A. M. S. Mendes, "Multistage predictive current control based on virtual vectors for the reduction of current harmonics in six-phase PMSMs," *IEEE Trans. Energy Convers.*, vol. 36, no. 2, pp. 1368–1377, Jun. 2021.

[14] Y. Zhang, W. Xie, Z. Li, and Y. Zhang, "Model predictive direct power control of a PWM rectifier with duty cycle optimization," *IEEE Trans. Power Electron.*, vol. 28, no. 11, pp. 5343–5351, Nov. 2013.

[15] Y. Zhang and H. Yang, "Model predictive torque control of induction motor drives with optimal duty cycle control," *IEEE Trans. Power Electron.*, vol. 29, no. 12, pp. 6593–6603, Dec. 2014.

[16] A. Gonzalez-Prieto, C. Martin, I. González-Prieto, M. J. Duran, J. Carrillo-Ríos, and J. J. Aciego, "Hybrid multivector FCS–MPC for six-phase electric drives," *IEEE Trans. Power Electron.*, vol. 37, no. 8, pp. 8988–8999, Aug. 2022.

[17] T. Tao, W. Zhao, Y. He, J. Zhu, H. Tan, and R. Xue, "Multivector predictive current control for five-phase PM motor by using hybrid duty modulation technology," *IEEE Trans. Transp. Electrific.*, vol. 6, no. 4, pp. 1603–1612, Dec. 2020.

[18] Z. Zhang, H. Fang, F. Gao, J. Rodríguez, and R. Kennel, "Multiple-vector model predictive power control for grid-tied wind turbine system with enhanced steady-state control performance," *IEEE Trans. Ind. Electron.*, vol. 64, no. 8, pp. 6287–6298, Aug. 2017.

[19] B. Shao et al., "Improved direct torque control method for dual-three-phase permanent-magnet synchronous machines with back EMF harmonics," *IEEE Trans. Ind. Electron.*, vol. 68, no. 10, pp. 9319–9333, Oct. 2021.

[20] B. Shao, Z. Q. Zhu, J. Feng, S. Guo, Y. Li, and W. Liao, "Compensation of selective current harmonics for switching-table-based direct torque control of dual three-phase PMSM drives," *IEEE Trans. Ind. Appl.*, vol. 57, no. 3, pp. 2505–2515, May/Jun. 2021.

[21] J. Xu, M. Odavic, Z.-Q. Zhu, Z.-Y. Wu, and N. Freire, "Switching-table-based direct torque control of dual three-phase PMSMs with closed-loop current harmonics compensation," *IEEE Trans. Power Electron.*, vol. 36, no. 9, pp. 10645–10659, Sep. 2021.

[22] C. Xiong, H. Xu, T. Guan, and P. Zhou, "A constant switching frequency multiple-vector-based model predictive current control of five-phase PMSM with nonsinusoidal back EMF," *IEEE Trans. Ind. Electron.*, vol. 67, no. 3, pp. 1695–1707, Mar. 2020.

[23] H. S. Che, M. J. Duran, E. Levi, M. Jones, W.-P. Hew, and N. A. Rahim, "Postfault operation of an asymmetrical six-phase induction machine with single and two isolated neutral points," *IEEE Trans. Power Electron.*, vol. 29, no. 10, pp. 5406–5416, Oct. 2014.
[24] Y. Hu, Y. Feng, and X. Li, "Fault-tolerant hybrid current control of dual three-phase PMSM with one phase open," *IEEE J. Emerg. Sel. Topics Power Electron.*, vol. 10, no. 3, pp. 3418–3426, Jun. 2022.
[25] W. N. W. A. Munim, M. J. Duran, H. S. Che, M. Bermúdez, I. González-Prieto, and N. A. Rahim, "A unified analysis of the fault tolerance capability in six-phase induction motor drives," *IEEE Trans. Power Electron.*, vol. 32, no. 10, pp. 7824–7836, Oct. 2017.
[26] Y. Zhao and T. A. Lipo, "Modeling and control of a multi-phase induction machine with structural unbalance part I. Machine modeling and multi-dimensional current regulation," *IEEE Trans. Energy Convers.*, vol. 11, no. 3, pp. 570–577, Sep. 1996.
[27] H. Guzman, M. J. Duran, F. Barrero, B. Bogado, and S. Toral, "Speed control of five-phase induction motors with integrated open-phase fault operation using model-based predictive current control techniques," *IEEE Trans. Ind. Electron.*, vol. 61, no. 9, pp. 4474–4484, Sep. 2014.
[28] T. Tao, W. Zhao, Y. He, Y. Cheng, S. Saeed, and J. Zhu, "Enhanced fault-tolerant model predictive current control for a five-phase PM motor with continued modulation," *IEEE Trans. Power Electron.*, vol. 36, no. 3, pp. 3236–3246, Mar. 2021.
[29] B. Chikondra, U. R. Muduli, and R. K. Behera, "An improved open-phase fault-tolerant DTC technique for five-phase induction motor drive based on virtual vectors assessment," *IEEE Trans. Ind. Electron.*, vol. 68, no. 6, pp. 4598–4609, Jun. 2021.
[30] H. Wang, X. Zheng, X. Yuan, and X. Wu, "Enhanced natural fault-tolerant model predictive current control in nine-phase motor drives under open-phase faults," *IEEE Trans. Energy Convers.*, to be published, doi: 10.1109/TEC.2022.3179735.
[31] I. González-Prieto, M. J. Durán, M. Bermúdez, F. Barrero, and C. Martín, "Assessment of virtual-voltage-based model predictive controllers in six-phase drives under open-phase faults," *IEEE J. Emerg. Sel. Topics Power Electron.*, vol. 8, no. 3, pp. 2634–2644, Sep. 2020.
[32] Y. Luo and C. Liu, "Pre- and post-fault tolerant operation of a six-phase PMSM motor using FCS-MPC without controller reconfiguration," *IEEE Trans. Veh. Technol.*, vol. 68, no. 1, pp. 254–263, Jan. 2019.
[33] Y. Hu, Z. Q. Zhu, and Z. Wu, "Modelling and vector control of dual three-phase PMSM with one-phase open," *IET Electr. Power Appl.*, vol. 15, pp. 847–860, Apr. 2021.

**Jia Cui** received the M.Sc. degree in control science and engineering from the Jiangsu University of Science and Technology, Zhenjiang, China, in 2019. He is currently working toward the Ph.D. degree in electrical engineering with Jiangsu University, Zhenjiang, China.

His research interest includes design and control of electric machine and drive.

**Jinghua Ji** received the B.Sc., M.Sc., and Ph.D. degrees in electrical engineering from Jiangsu University, Zhenjiang, China, in 2000, 2003, and 2009, respectively.

Since 2000, she has been with the School of Electrical and Information Engineering, Jiangsu University, where she is currently a Professor. From 2013 to 2014, she was a Visiting Scholar with the Department of Electronic and Electrical Engineering, University of Sheffield, Sheffield, U.K. She has authored or coauthored more than 50 technical papers in the given areas. Her research interests include electrical machines and motor drives.

**Wenxiang Zhao** (Senior Member, IEEE) received the B.Sc. and M.Sc. degrees from Jiangsu University, Zhenjiang, China, in 1999 and 2003, respectively, and the Ph.D. degree from Southeast University, Nanjing, China, in 2010, all in electrical engineering.

Since 2003, he has been with Jiangsu University, where he is currently a Professor with the School of Electrical Information Engineering. From 2008 to 2009, he was a Research Assistant with the Department of Electrical and Electronic Engineering, University of Hong Kong, Hong Kong. From 2013 to 2014, he was a Visiting Professor with the Department of Electronic and Electrical Engineering, University of Sheffield, Sheffield, U.K. He has authored and coauthored more than 150 papers published in various IEEE Transactions. His current research interests include electric machine design, modeling, fault analysis, and intelligent control.

**Tao Tao** received the B.Sc. degree from Nanjing Agricultural University, Nanjing, China, in 2009, and the Ph.D. degree from Jiangsu University, Zhenjiang, China, in 2020, both in electrical engineering.

Since 2021, he has been with Jiangsu University, where he is currently a Lecturer with the School of Electrical Information Engineering. His research interest includes control of multiphase permanent-magnet machines.

**Linsen Huang** received the M.Sc. degree in electrical engineering from the Hunan University of Technology, Zhuzhou, China, in 2015. He is currently working toward the Ph.D. degree in electrical engineering with Jiangsu University, Zhenjiang, China.

His research interests include electric machine control and power electronic converter.

**Hongyu Tang** received the B.Sc. degree from the Jiangsu University of Science and Technology, Zhenjiang, China, in 1999, and the M.Sc. degree from Jiangsu University, Zhenjiang, China, in 2005, both in electrical engineering.

Since 1999, he has been with Zhenjiang College, Zhenjiang, China, where he is currently a Professor with the School of Electrical and Information. His current research interest includes analysis and control of permanent-magnet motor drive systems.